

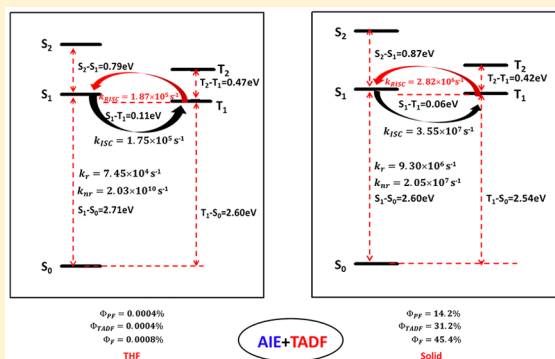
Excited State Properties of a Thermally Activated Delayed Fluorescence Molecule in Solid Phase Studied by Quantum Mechanics/Molecular Mechanics Method

Jianzhong Fan,¹ Yuchen Zhang, Yong Zhou, Lili Lin,^{2*} and Chuan-Kui Wang^{2*}

Shandong Province Key Laboratory of Medical Physics and Image Processing Technology, Institute of Materials and Clean Energy, School of Physics and Electronics, Shandong Normal University, 250014 Jinan, China

Supporting Information

ABSTRACT: Excited state properties of a thermally activated delayed fluorescence molecule (4-(10*H*-phenoxazin-10-yl)phenyl)(dibenzo-*[b,d]*thiophen-2-yl)methanone (DBT-BZ-PXZ) are theoretically studied in liquid (tetrahydrofuran (THF)) and solid phases, respectively. Solvent environment in THF is considered by polarizable continuum model (PCM) and the molecule in solid phase is investigated by a combined quantum mechanics and molecular mechanics (QM/MM) method. Results show that the geometrical changes between ground state (S_0) and lowest singlet excited state (S_1) are hindered in solid phase by the restricted intramolecular rotation (RIR) and restricted intramolecular vibration (RIV) effects, which brings smaller values of Huang–Rhys (HR) factors and reorganization energies compared to those in liquid phase. Thus, nonradiative energy consumptions are suppressed and enhanced fluorescent efficiency is found in solid phase. The calculated prompt fluorescence efficiency (Φ_{Prompt}) and delayed fluorescence efficiency (Φ_{TADF}) in solid phase are 14.2% and 31.2% respectively, which demonstrates the aggregation induced emission (AIE) mechanism for DBT-BZ-PXZ. Moreover, temperature dependence of the reverse intersystem crossing (RISC) rate is theoretically illustrated. Furthermore, a hybridized local and charge transfer (HLCT) property of the lowest triplet excited state (T_1) is found. This transition feature brings a large spin–orbit coupling (SOC) constant and a small energy gap (ΔE_{st}) between S_1 and T_1 , which facilitates the RISC process. Our calculations give reasonable explanation for the previous experimental measurements and provide underlying perspectives for nonradiative assumptions of excited state energy.



1. INTRODUCTION

Recently, organic light emitting diodes (OLEDs) have attracted significant attention as next generation full color display devices, and they are beginning to be widely used in mobile phones, OLED television sets and solid-state lighting sources.^{1–3} According to spin statistics, the singlet and triplet excitons are generated with the ratio of 1:3.^{4–6} For conventional fluorescent OLEDs, only singlet excitons (25%) can be used and all triplet excitons (75%) are wasted, this brings low internal quantum efficiency (IQE) for fluorescent OLEDs. In contrast, phosphorescent OLEDs can achieve full exciton utilization due to the strong spin orbit coupling enabled by the presence of heavy metal atoms such as iridium and platinum.^{7–10} However, the phosphorescent materials are limited to Ir and Pt complexes, thus both fluorescence and phosphorescence OLEDs have advantages and disadvantages. Until 2012, Adachi's group successfully achieves 100% IQE by the use of pure organic thermally activated delayed fluorescence (TADF) OLEDs.^{11–13} TADF is a promising mechanism for converting triplet excitons to singlet states by the reverse intersystem crossing (RISC) from lowest triplet excited state (T_1) to lowest singlet excited state (S_1) under thermal activation. According to the equation $k_{\text{RISC}} \approx \exp(-\Delta E_{\text{st}}/$

$k_{\text{B}}T)$ where k_{B} is the Boltzmann constant, T is the temperature and ΔE_{st} is the energy gap between S_1 and T_1 , we know a small ΔE_{st} plays an important role in realizing fast RISC.¹⁴ According to the equation $\Delta E_{\text{st}} = 2 \iint \Phi_{\text{L}}(1) \Phi_{\text{H}}(2) \frac{e^2}{r_{12}} \Phi_{\text{L}}(2) \Phi_{\text{H}}(1) dr_1 dr_2$, one effective way to obtain a small ΔE_{st} is decreasing the overlap between highest occupied molecular orbital (HOMO) and lowest unoccupied molecular orbital (LUMO), success has been achieved in many previous works.¹⁵ However, a stubborn problem for TADF materials in practical application is that most TADF emitters suffer from aggregation-caused quenching (ACQ) in solid phase. Thus, TADF emitters have to be dispersed into host matrices to suppress the effect of ACQ and exciton annihilation.^{16,17} Fortunately, Tang et al. find the aggregation-induced emission (AIE) materials which show a wide application in medicine and biology and so on.¹⁸ Furthermore, TADF materials with AIE feature show promising applications in optoelectronic devices and corresponding

Received: October 16, 2017

Revised: December 29, 2017

Published: January 8, 2018

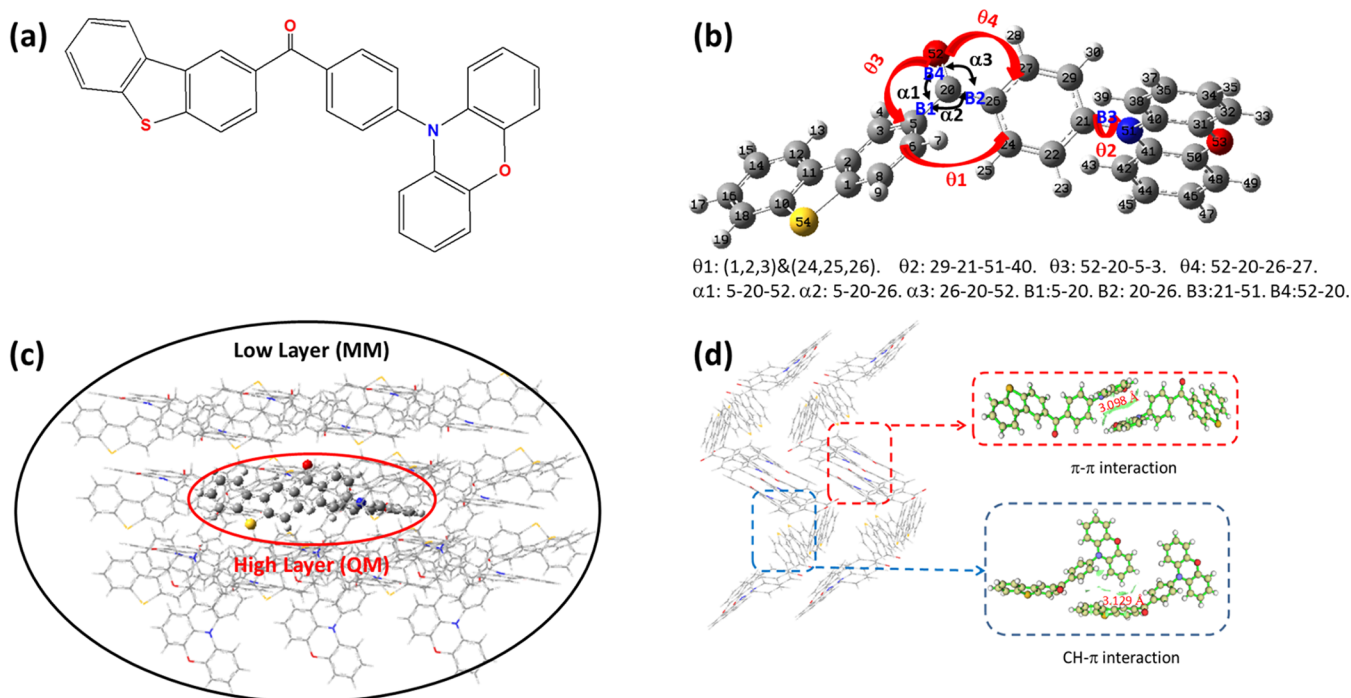


Figure 1. (a) Chemical structure of DBT-BZ-PXZ. (b) Atomic labels, interesting bond lengths, bond angles, and dihedral angles. (c) ONIOM model: surrounding molecules are regarded as the low layer and the centered DBT-BZ-PXZ is treated as the high layer. (d) Intermolecular interactions of the DBT-BZ-PXZ crystal.

investigations become research hotspots because these AIE-TADF-OLEDs are anticipated to contribute to high efficiency, low roll-off, and low-cost nondoped OLEDs.^{19–22} However, the mechanisms of TADF and AIE are still unclear. Fundamental factors that lead to enhanced emission of dyes in viscous and solid state environments are of ongoing interest.

In this work, we perform a detailed study on the latest reported TADF molecule (4-(10*H*-phenoxazin-10-yl)phenyl)-(dibenzo[*b,d*]thiophen-2-yl)methanone (DBT-BZ-PXZ) based on first-principles calculations. DBT-BZ-PXZ exhibits prominent AIE and TADF properties, and remarkably high performance electroluminescence (EL) efficiency with small efficiency roll-off is detected.²³ Photophysical properties of DBT-BZ-PXZ in tetrahydrofuran (THF) solution is theoretically investigated by using the polarizable continuum model (PCM).²⁴ Besides, in order to take the environment effect of the molecule in film into consideration, the combined quantum mechanics and molecular mechanics (QM/MM) method is adopted.^{25–28} Furthermore, the nonradiative rate as well as the intersystem crossing (ISC) rate and reverse intersystem crossing (RISC) rate are calculated based on the thermal vibration correlation function (TVCF). Finally, the excited state dynamics for DBT-BZ-PXZ with TADF and AIE mechanisms in solid phase is illustrated, and the experimental measurements are reasonably elucidated.

2. THEORETICAL METHOD

For TADF systems, the total fluorescence efficiency (Φ_F) includes prompt fluorescence (PF) efficiency (Φ_{PF}) and thermally activated delayed fluorescence (TADF) efficiency (Φ_{TADF}). The photoluminescence (PL) quantum efficiencies of PF and TADF can be written as $\Phi_{PF} = \frac{k_r}{k_r + k_{nr} + k_{ISC}}$ and $\Phi_{TADF} = \frac{\Phi_{ISC} \Phi_{RISC}}{1 - \Phi_{ISC} \Phi_{RISC}} \Phi_{PF}$, where Φ_{ISC} and Φ_{RISC} are the

intersystem crossing (ISC) efficiency and reverse intersystem crossing (RISC) efficiency, respectively.²⁹ Schematic of the different transition processes is shown in Figure S1, k_r is the radiative decay rate from S_1 to ground state (S_0), k_{nr} is the nonradiative decay rate from S_1 to S_0 and k_{ISC} is the ISC rate from S_1 to T_1 . Thus, in order to obtain the luminescence efficiency, we should first calculate the rate parameters.

The radiative decay rate is calculated by Einstein spontaneous emission equation as follows

$$k_r = \frac{f \Delta E_{fi}^2}{1.499} \quad (1)$$

Here f is oscillator strength and ΔE_{fi} is the vertical emission energy with the unit of wavenumber (cm^{-1}).

As for the nonradiative decay rate, it is deduced based on first-order perturbation theory and the Fermi's golden rule (FGR)

$$k_{nr} = \frac{2\pi}{\hbar^2} \sum_{u,v} P_{iv} |H_{fu,iv}|^2 \delta(E_{iv} - E_{fu}) \quad (2)$$

Here P_{iv} is the initial state Boltzmann distribution function and H is the interaction between two different Born–Oppenheimer states, it contains two components

$$\hat{H}\Psi_{iv} = \hat{H}^{BO}\Phi_i(r, Q)\Theta_{iv}(Q) + \hat{H}^{SO}\Phi_i(r, Q)\Theta_{iv}(Q) \quad (3)$$

Here \hat{H}^{BO} is the nonadiabatic coupling and \hat{H}^{SO} denotes the spin–orbit coupling. The nonradiative decay rate constant from S_1 to S_0 can be written as

$$k_{nr} = \frac{2\pi}{\hbar} \sum_{kl} R_{kl} Z_i^{-1} \sum_{vu} e^{-\beta E_{iv}} \langle \Theta_{fu} | \hat{p}_{jk} | \Theta_{iv} \rangle \langle \Theta_{iv} | \hat{p}_{jl} | \Theta_{fu} \rangle \delta(E_{iv} - E_{fu}) \quad (4)$$

Here $R_{kl} = \langle \Phi_f | \hat{p}_{fk} | \Phi_i \rangle \langle \Phi_i | \hat{p}_{fl} | \Phi_j \rangle$ is the nonadiabatic electronic coupling. Z_i is the partition function. $\hat{p}_{fk} = -i\hbar \frac{\partial}{\partial Q_{fk}}$ represents the normal momentum operator of the k th normal mode in the final electronic state. Following the equations $L_{f\delta j, k} = \frac{\partial q_{\delta j}}{\partial Q_{fk}}$ and $q_{\delta j} = \sqrt{M_\delta} R_{\delta j}$, where R_j is the Cartesian coordinate of the δ th atom along the j th direction, the electronic coupling term at the equilibrium position is

$$\langle \Phi_f | \hat{p}_{fk} | \Phi_i \rangle = -i\hbar \left\langle \Phi_f \left| \frac{\partial}{\partial Q_{fk}} \right| \Phi_i \right\rangle = -i\hbar \frac{\Phi_f^0 \left| \frac{\partial U}{\partial Q_{fk}} \right| \Phi_i^0}{E_i^0 - E_f^0} \quad (5)$$

U is the electron–nuclear potential term in the Hamiltonian. $\left\langle \Phi_f^0 \left| \frac{\partial U}{\partial Q_{fk}} \right| \Phi_i^0 \right\rangle = -\sum_\delta \frac{Z_\delta e^2}{\sqrt{M_\delta}} \sum_{\tau=x,y,z} E_{i \rightarrow f, \delta \tau} L_{\delta \tau, k}$, $E_{i \rightarrow f, \delta \tau}$ is the transition electric field and it can be calculated by time-dependent density functional theory directly. On the basis of the Franck–Condon principle and applying the Fourier transform of the delta function, the eq 4 can be written as

$$k_{nr} = \sum_{kl} \frac{1}{\hbar^2} R_{kl} \int_{-\infty}^{\infty} dt [e^{i\omega_f t} Z_i^{-1} \rho_{ic, kl}(t, T)] \quad (6)$$

Here $\rho_{ic, kl}(t, T)$ is the thermal vibration correlation function (TVCF) and it can be expressed as $\rho_{ic, kl}(t, T) = \text{Tr}(\hat{p}_{fk} e^{-i\tau_f \hat{H}_f} \hat{p}_{fl} e^{-i\tau_i \hat{H}_i})$. Similarly, the intersystem crossing rate constant between two electronic states with different spin states is written as

$$k_{ISC} = \frac{1}{\hbar} \langle \Phi_f | \hat{H}^{SO} | \Phi_i \rangle \int_{-\infty}^{\infty} dt [e^{i\omega_f t} Z_i^{-1} \rho_{ISC}(t, T)] \quad (7)$$

Both the methodology and application of this formalism can be found in Peng's and Shuai's works.^{30–32} Besides, the vibration-mode mixing effect can be taken into accounts as $Q_{ik} = \sum_l^{3n-6} S_{kl} Q_{fl} + D_k$. Here, S is the Duschinsky rotation matrix representing the mixing of normal modes in the initial and final states and the vector D_k is the displacement along the normal mode k . All these parameters and reorganization energies can be projected onto the internal coordinate by Reimers' algorithm.³³

3. COMPUTATIONAL DETAILS

The ground state geometry of DBT-BZ-PXZ (as shown in Figure 1a) is optimized by density functional theory (DFT) method and the photophysical properties of excited states are studied by time-dependent density functional theory (TD-DFT). The properties of excited states are functionals dependent especially for donor–acceptor type structures. Thus, an optimal functional should be determined for our investigated DBT-BZ-PXZ. On the basis of the ground state structure, some ingenious approaches such as LC-wPBE method, LC-BLYP method, NTO method and optimal Hartree–Fock (OHF) method are proposed and well applied to calculate the S_1 – T_1 gap for TADF molecules.^{34–39} In this work, the emission wavelength of the DBT-BZ-PXZ in solid phase is calculated by using different functional with different percentage of HF exchange (HF%), corresponding data are

listed in Table 1. The emission wavelength of the DBT-BZ-PXZ in solid state is 528 nm calculated by BMK functional,

Table 1. Emission wavelengths calculated by adopting different functionals for molecule in solid phase are listed

	HF (%)	solid (nm)
O3LYP	11.61	1085
B3LYP	20	757
PBE0	25	680
BMK	42	528
M062X	54	462
wB97XD	—	419
exp ^a	—	549

^aExp is experimental data.

which is in better agreement with the experimental value (549 nm in the neat film). Consequently, the BMK functional with 6-31G(d) basis set is adopted in our following calculations.

In order to investigate the case in solid phase, we perform calculations by using the combined quantum mechanics and molecular mechanics (QM/MM) method with two-layer ONIOM approach.⁴⁰ The computational model is built based on the X-ray crystal structure as shown in Figure 1c. The central single molecule is regarded as high layer and calculated by QM method. The surrounding molecules are treated as MM part which is defined as the low layer. The universal force field (UFF) is adopted for the MM part and the electronic embedding is selected in our QM/MM calculations. Besides, molecules of MM part are frozen during the QM/MM geometry optimizations for S_0 , S_1 and T_1 states. All these calculations are performed in Gaussian 09 package.⁴¹

On the basis of the calculated electronic structure data, the normal-mode analyses are carried out by the DUSHIN program.³³ Furthermore, the nonradiative decay rate from S_1 to S_0 , ISC and RISC rates between S_1 and T_1 in THF and solid phase are all calculated by MOMAP (Molecular Materials Property Prediction Package) which shows superiority in describing and predicting the optical properties of the polyatomic molecules.

4. RESULTS AND DISCUSSIONS

4.1. Molecular Geometries. Molecular geometry determines both the electronic structures and photophysical properties. Thus, the geometric structures of DBT-BZ-PXZ for S_0 , S_1 and T_1 states are both theoretically studied in THF and solid phase by BMK functional with 6-31G(d) basis set. Detailed parameters for interesting bond lengths, bond angles and dihedral angles (marked in Figure 1b) are collected in Table 2. Comparing data of S_0 and S_1 in THF and in solid phase respectively, we know that the dihedral angle of θ_2 and θ_4 changes 10.9° and 18.9° respectively in THF, and these changes become 12.5° and 7.9° in solid phase. Thus, the rotation motion of θ_4 is restricted in solid phase by the intermolecular interaction which is shown in Figure 1d measured by the reduced density gradient (RDG) function which is expressed as $\text{RDG}(r) = \frac{1}{2(3\pi^2)^{1/3}} \frac{|\nabla \rho(r)|}{\rho(r)^{4/3}}$, where $\rho(r)$ is the total electron density.⁴² In this calculation, a dimer is selected from crystal data and calculated by QM method with the consideration of dispersion effect. Remarkable intermolecular π – π interaction between two PXZ units and CH– π interaction between PXZ and DBT units can be found through

Table 2. Geometry Parameters of S_0 , S_1 , and T_1 States in THF and Solid Phase^a

	DBT-BZ-PXZ										exp
	THF					solid					
	S ₀	S ₁	T ₁	Δ _{S0-S1}	Δ _{S1-T1}	S ₀	S ₁	T ₁	Δ _{S0-S1}	Δ _{S1-T1}	
θ ₁	51.2	44.1	44.6	7.1	0.5	62.6	56.3	60.8	6.3	4.5	61.6
θ ₂	79.2	90.1	58.1	10.9	32.0	64.1	76.6	65.9	12.5	10.7	65.5
θ ₃	25.0	32.7	32.6	7.7	0.1	43.9	43.2	45.4	0.7	2.2	47.8
θ ₄	27.7	8.8	9.9	18.9	1.1	16.1	8.2	11.7	7.9	3.5	10.5
α ₁	120.2	117.2	117.6	3.0	0.4	120.3	119.0	119.1	1.3	0.1	119.9
α ₂	120.3	120.9	121.1	0.6	0.2	118.5	118.4	118.3	0.1	0.1	119.1
α ₃	119.5	121.9	121.3	2.4	0.6	121.2	122.6	122.6	1.4	0.0	121.0
B ₁	1.505	1.513	1.512	0.008	0.001	1.508	1.512	1.514	0.004	0.002	1.496
B ₂	1.509	1.448	1.449	0.061	0.001	1.501	1.452	1.450	0.049	0.002	1.489
B ₃	1.426	1.427	1.407	0.001	0.020	1.421	1.442	1.426	0.021	0.016	1.429
B ₄	1.219	1.255	1.253	0.036	0.002	1.217	1.248	1.246	0.031	0.002	1.221

^a θ , α , and B (marked in Figure 1b) represent the dihedral angle, bond angle and bond length, respectively. Δ represents the variation between two states.

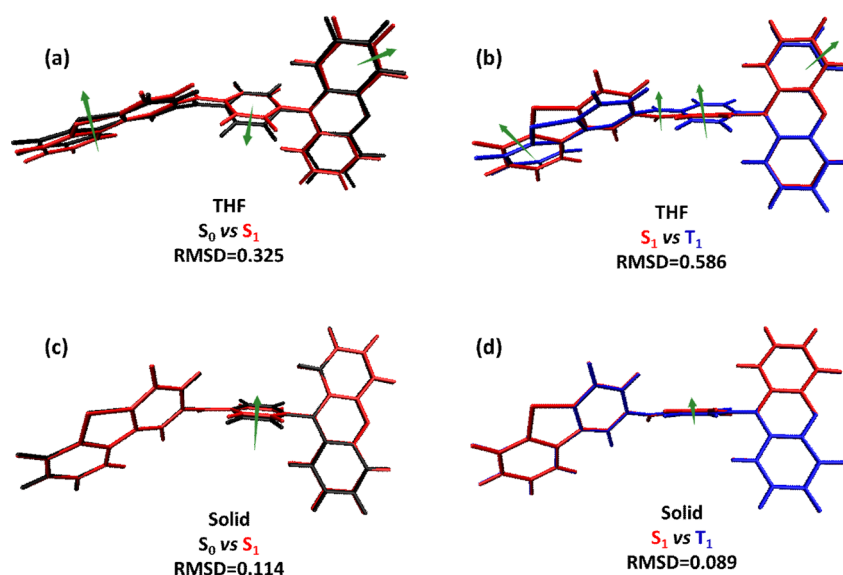
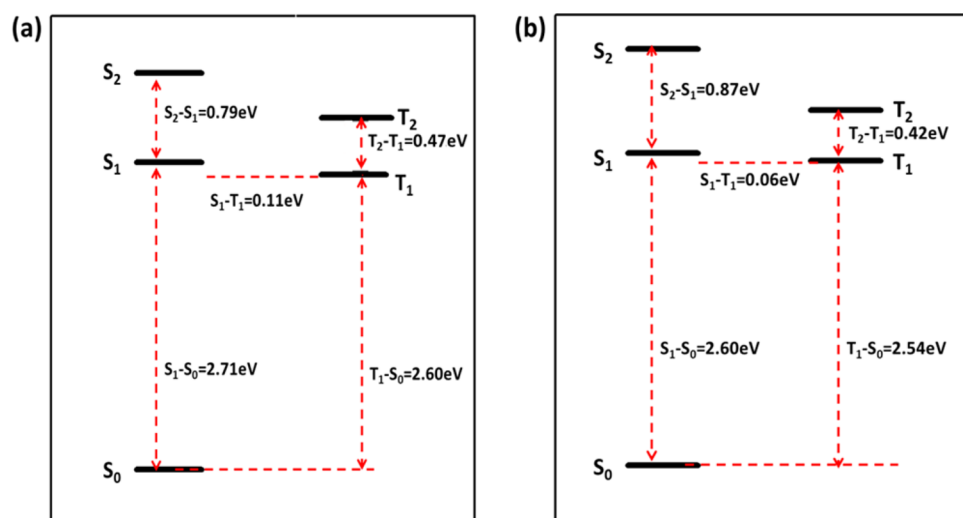
Figure 2. Geometry comparisons between S_0 (black), S_1 (red) and T_1 (blue) in THF (a, b) and solid phase (c, d).

Figure 3. Adiabatic excitation energies for DBT-BZ-PXZ in THF (a) and the solid phase (b), respectively.

analyzing the crystal. Besides, the variation of central C=O unit is hindered in solid through analyzing the changes of bond length and bond angle in THF and solid phase, respectively. The root of the mean of squared displacement (RMSD) with the expression

$$\text{RMSD} = \sqrt{\frac{1}{N} \sum_i^{\text{atom}} [(x_i - x'_i)^2 + (y_i - y'_i)^2 + (z_i - z'_i)^2]}, \text{ is an}$$

effective tool to quantitatively characterize the geometric changes, and the value of RMSD between two states is calculated by Multiwfn.⁴³ It is found that the geometric changes between S_0 and S_1 in THF are more significant than that in solid phase with the RMSD value is 0.325 Å and 0.114 Å respectively shown in parts a and c of Figure 2. Thus, the nonradiative energy consumption path is hindered and enhanced fluorescence efficiency can be expected in solid phase. In order to illustrate the influence of molecular surrounding environment on S_1 and T_1 geometries, RMSD is calculated and comparisons are shown in Figure S2. Large values of RMSD and obvious changes can be found. This means the necessity of investigation for molecule in solid phase. Furthermore, for investigating the ISC and RISC processes, the geometry parameters are compared between S_1 and T_1 states. In THF, θ_2 changes 32° when molecule transfers from S_1 to T_1 , and a restricted rotation is found in solid phase with the change of θ_2 decreases to 10.7°. The central C=O unit is slightly changed. Besides, visible comparisons between S_1 and T_1 in THF and solid phase are shown in Figure 2b and 2d, the value of RMSD in solid phase is 0.089 Å which is much smaller than that in THF (RMSD = 0.586 Å) and this indicates a small variation of the reorganization energy for the ISC and RISC processes. In order to provide benchmarking results, calculations with the consideration of dispersion (BMK-GD3BJ) are carried out and corresponding data are collected in Table S1. Different geometry changes in the transition process in THF and solid phase are shown to have close relationship with the photophysical properties in the following section.

4.2. Energy Gap and Transition Property. For TADF molecules, the energy gap (ΔE_{st}) between S_1 and T_1 plays an important role for the RISC process. Thus, the adiabatic excitation energies for DBT-BZ-PXZ in THF and solid phase are calculated as shown in Figure 3. The calculated ΔE_{st} is 0.11 eV in THF and it decreases to 0.06 eV in solid phase. Moreover, it is corresponding well with the experimental value (0.09 eV) that is determined from the onsets of fluorescence spectra at room temperature and phosphorescence spectra at 77 K. As Gibson and Penfold point out, the vibronic coupling effect between the lowest local excitation triplet (^3LE) and lowest charge transfer triplet (^3CT) can facilitate the RISC for TADF.^{44,45} No additional energy level is found between S_1 and T_1 for DBT-BZ-PXZ. Thus, this effect can be neglected.

Moreover, the transition properties of excited states play an important role in determining the excited state properties. Natural transition orbital (NTO) analyses of S_1 and T_1 in THF and solid phase are performed respectively, and the highest occupied natural transition orbital (HONTO) and the lowest unoccupied natural transition orbital (LUNTO) are calculated. As shown in Figure 4, HONTO and LUNTO predominates the transition for S_1 and T_1 . As for S_1 , it is a typical charge transfer (CT) state with the HONTO is localized in PXZ unit and LUNTO is mainly distributed on the BZ unit, such efficient separation between HONTO and LUNTO brings small ΔE_{st} (0.06 eV). However, for T_1 , a hybridized local and charge

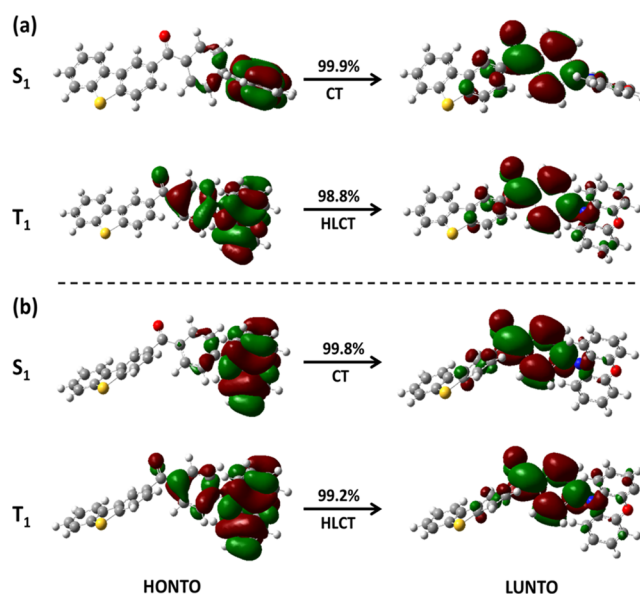


Figure 4. Transition characteristics for S_1 and T_1 states of DBT-BZ-PXZ in THF (a) and solid phase (b), respectively (isovalue = 0.02). The value above every arrow represents the ratio of depicted NTOs in the corresponding transition.

transfer (HLCT) feature can be seen both in THF and solid phase with remarkable overlap between HONTO and LUNTO in BZ unit. Previous investigations show that the ^3LE often brings a stable triplet state with enhanced RISC from ^3LE to ^1CT , and ^3CT can result a small energy gap between ^1CT and ^3CT .⁴⁶ Thus, the HLCT state possesses the advantage of ^3LE and ^3CT , and efficient RISC process from T_1 to S_1 can be expected.

4.3. Huang–Rhys Factor and Reorganization Energy.

Huang–Rhys (HR) factor and reorganization energy are two effective parameters to measure the nonradiative consumption of excited state energy. Schematic representation of the adiabatic potential energy surfaces (PES) for S_0 and S_1 is shown in Figure S3. Reorganization energy is calculated by normal mode (NM) method with the consideration of zero-point energy (ZPE) corrections. To figure out the structure–property relationship during the energy conversion process from S_1 to S_0 , the HR factors are first calculated according to the equation $\text{HR}_k = \frac{\omega_k D_k^2}{2}$. Here, ω_k represents the vibration frequency and D_k is the normal coordinate displacement of mode k . Then, HR factors versus the normal-mode frequencies in THF and solid phase are drawn in Figure 5a and 5b. For DBT-BZ-PXZ in THF, the large values of HR factor are all in low frequency regions ($<200 \text{ cm}^{-1}$) such as 1.46 (13.30 cm^{-1}), 3.64 (21.31 cm^{-1}), 2.33 (52.78 cm^{-1}), and 1.97 (92.54 cm^{-1}) which correspond to the rotation of dihedral angles as shown in the insets. While for DBT-BZ-PXZ in solid phase, HR factors are all decreased with the largest one is 2.00 (68.55 cm^{-1}). Thus, geometry variations are restricted by the intermolecular interaction in solid phase and this result is corresponding well with the above geometry analysis in section 4.1 with a decreased RMSD is 0.114 Å in solid phase compared with that in THF (RMSD = 0.325 Å). Nonradiative energy consumptions can be suppressed due to aggregation and enhanced fluorescent efficiency can be expected in the solid phase. Besides, the reorganization energies versus the normal-mode frequencies in THF and solid phase are shown in Figure 5,

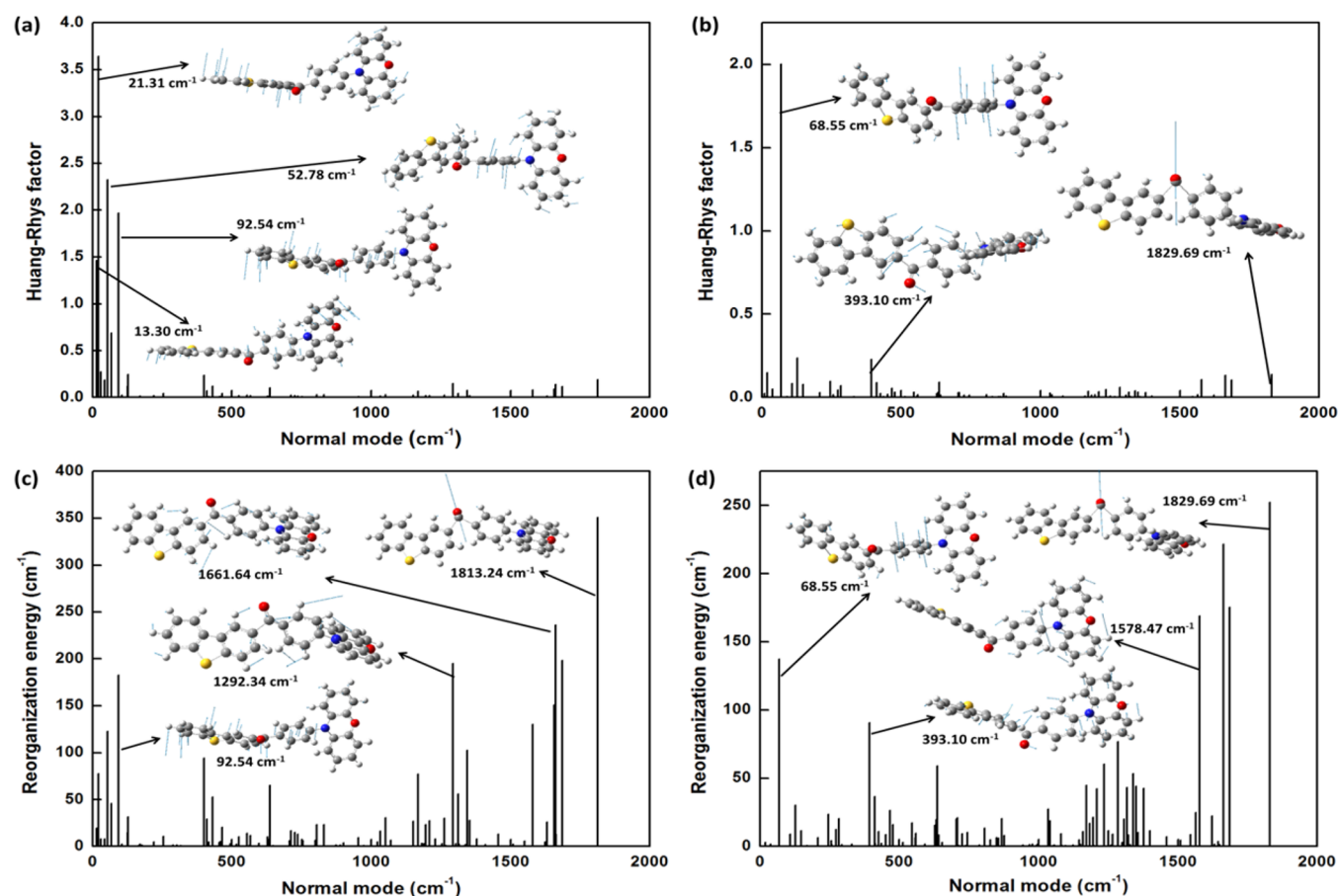


Figure 5. Calculated HR factors versus the normal-mode frequencies in THF (a) and solid phase (b) as well as the reorganization energies versus the normal-mode frequencies in THF (c) and solid phase (d), respectively. Representative vibration modes are shown as insets.

parts c and d. The largest one comes from C=O bond vibration both in THF (1813.24 cm⁻¹) and solid phase (1829.69 cm⁻¹), and remarkable reduction can be found both in low and high frequency regions.

Furthermore, in order to better illustrate the relationship between molecular geometry and nonradiative energy dissipation, the reorganization energies are all projected onto the internal coordinate both in THF and solid phase. The contributions from bond length, bond angle and dihedral angle are shown in Figure 6, and corresponding data are collected in Table 3. Results show that the bond length contribution to reorganization energies takes the major part with the ratio 67.4% (237.1 meV) in THF and 70.1% (196.8 meV) in solid phase, respectively. Besides this, the decreased reorganization energy (70.8 meV) from THF to solid phase mainly comes from the decrement contributed by bond length (40.3 meV) and dihedral angle (29.4 meV), and all of these changes are related to the motion of central C=O unit.

Thus, from detailed analysis for HR factors and reorganization energies in THF and solid phase as well as their changes from THF to solid phase, we know that two kinds of mode are responsible for the nonradiative decay: one is the low frequency twisting motion of dihedral angle θ_4 and the other is the high frequency stretching motion of bond length B_4 . All these motions are effectively hindered through the restricted intramolecular rotation (RIR) effect and restricted intramolecular vibration (RIV) effect, respectively. So, the non-radiative energy consumptions of the excited state are hindered in solid phase, and the aggregation induced emission (AIE)

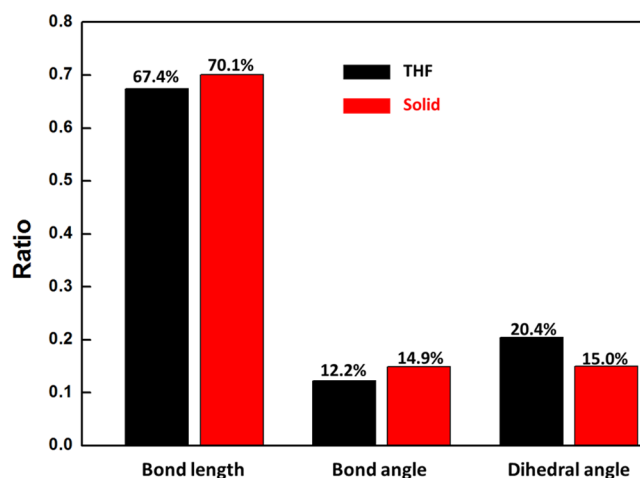


Figure 6. Contribution ratios to the reorganization energy from bond length, bond angle and dihedral angle of DBT-BZ-PXZ in THF and solid phase, respectively.

mechanism is revealed for DBT-BZ-PXZ; more evidence is provided in the following section.

4.4. Excited State Dynamics. In this section, the excited state dynamics of DBT-BZ-PXZ is illustrated, the prompt fluorescence and delayed fluorescence efficiency are calculated. As we know, the ISC and RISC processes are not only related to the adiabatic energy gap between S_1 and T_1 , but also have relationship with the spin-orbit coupling (SOC) between

Table 3. Reorganization Energies (meV) from the Bond Length, Bond Angle, and Dihedral Angle in THF and Solid Phase^a

	THF	solid	$\Delta_{\text{THF-Solid}}$
bond length	237.1	196.8	40.3
bond angle	42.9	41.8	1.1
dihedral angle	71.7	42.3	29.4
total	351.7	280.9	70.8

^a $\Delta_{\text{THF-Solid}}$ represents the energy difference between THF and solid phase.

singlet and triplet states. The SOC constants (with the unit of cm^{-1}) between S_1 and T_1 are calculated both in THF and solid phase by the Dalton 2013 package.⁴⁷ Corresponding data are collected in Table 4. Results show that the SOC constant based

Table 4. Calculated Spin Orbit Coupling Constants (cm^{-1}) between Selected S_1 and T_1 for DBT-BZ-PXZ in THF and the Solid Phase, Based on Their Optimized S_1 and T_1 Structures, Respectively

geometry	$\langle S_1 H_{\text{SO}} T_1 \rangle$ (cm^{-1})	
	THF	solid
S_1	0.025	0.437
T_1	0.757	0.700

on T_1 structure is 0.757 cm^{-1} in THF and 0.700 cm^{-1} in solid phase, and they are larger than that calculated based on S_1 geometry. This is related to the transition properties of T_1 . As illustrated in section 4.2, T_1 possesses the HLCT feature which can facilitate the conversion between S_1 and T_1 . Furthermore, we calculate the radiative and nonradiative decay rates from S_1 to S_0 , as well as the ISC and RISC rates between S_1 and T_1 both in THF and solid phase. Finally, the prompt fluorescence efficiency (Φ_{Prompt}), delayed fluorescence efficiency (Φ_{TADF}) and the total fluorescence efficiency (Φ_{F}) are obtained by the equation shown in theoretical method section. All calculated data and experiment values are listed in Table 5. It can be seen that the radiative decay rate in solid ($9.30 \times 10^6 \text{ s}^{-1}$) is about 2 orders of magnitude larger than that in THF ($7.45 \times 10^4 \text{ s}^{-1}$), this is caused by the enlarged transition dipole moment for DBT-BZ-PXZ in solid phase (2.09 D) compared with that in THF (0.19 D). Besides, the calculated nonradiative decay rate K_{nr} in solid phase ($2.05 \times 10^7 \text{ s}^{-1}$) is about 3 orders of magnitude smaller than that in THF ($2.03 \times 10^{10} \text{ s}^{-1}$). This is corresponding well with the restricted geometry changes and decreased HR factors and reorganization energies in solid phase. Moreover, the calculated ISC rate in solid phase ($3.55 \times 10^7 \text{ s}^{-1}$) is larger than that in THF ($1.75 \times 10^5 \text{ s}^{-1}$), and this is due to the decreased S_1 – T_1 gap and increased SOC constant in solid phase. Moreover, different molecular geometries of S_1 and T_1 bring different transition properties for S_1 (CT) and T_1 (HLCT), this further affects the RISC process. As for the RISC rate, the calculated value in solid phase is comparable with reported efficient TADF molecules, because of the large SOC constant (0.700 cm^{-1}) which is due to the HLCT feature of T_1 state. Thus, not only the S_1 – T_1 gap but also the transition property of T_1 plays an important role in realizing efficient RISC. On the basis of our calculated rate constants in solid phase, the values of Φ_{Prompt} , Φ_{TADF} and Φ_{F} are obtained. No emitting is found in THF, remarkable prompt fluorescence ($\Phi_{\text{Prompt}} = 14.2\%$) and delayed fluorescence ($\Phi_{\text{TADF}} = 31.2\%$)

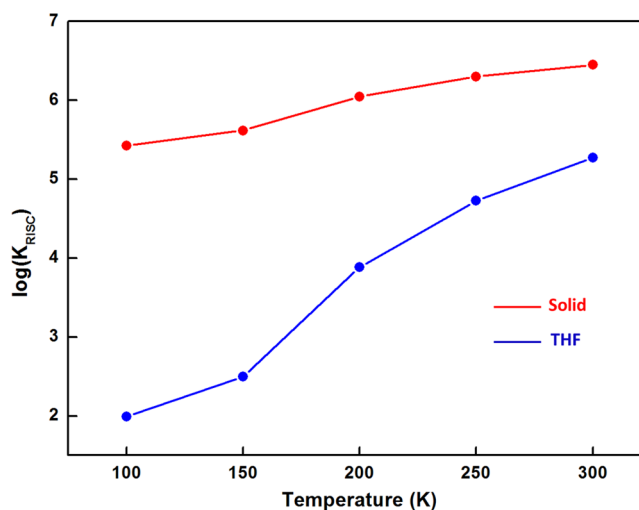
Table 5. Calculated Radiative and Non-Radiative rates (s^{-1}) from S_1 to S_0 as Well as the ISC and RISC Rates (s^{-1}) between S_1 and T_1 ^a

	THF	solid
$K_r (S_1 \rightarrow S_0)$	7.45×10^4	9.30×10^6
$K_{\text{nr}} (S_1 \rightarrow S_0)$	2.03×10^{10}	2.05×10^7
$K_{\text{ISC}} (S_1 \rightarrow T_1)$	1.75×10^5	3.55×10^7
$K_{\text{RISC}} (T_1 \rightarrow S_1)$	1.87×10^5	2.82×10^6
Φ_{Prompt}	0.0004%	14.2%
Φ_{TADF}	0.0004%	31.2%
Φ_{F}	0.0008%	45.4%
$K_r^{\text{exp}} (S_1 \rightarrow S_0)$	–	2.14×10^6
$K_{\text{nr}}^{\text{exp}} (S_1 \rightarrow S_0)$	–	3.48×10^6
$K_{\text{ISC}}^{\text{exp}} (S_1 \rightarrow T_1)$	–	2.05×10^7
$K_{\text{RISC}}^{\text{exp}} (T_1 \rightarrow S_1)^b$	–	9.95×10^6
$\Phi_{\text{prompt}}^{\text{exp}}$	–	8.2%
$\Phi_{\text{TADF}}^{\text{exp}}$	–	29.9%
$\Phi_{\text{F}}^{\text{exp}}$	–	38.1%

^aThe calculated prompt fluorescence efficiency (Φ_{Prompt}) and delayed efficiency (Φ_{TADF}) as well as the total fluorescence efficiency (Φ_{F}) are listed. Corresponding experimental results are also presented with the superscript “exp”.

$$^b K_{\text{RISC}}^{\text{exp}}(T_1 \rightarrow S_1) = \frac{K_{\text{TADF}}^{\text{exp}}}{1 - \frac{K_{\text{ISC}}^{\text{exp}}}{K_r^{\text{exp}} + K_{\text{nr}}^{\text{exp}} + K_{\text{ISC}}^{\text{exp}}}}$$

are generated in the solid phase. All these data are corresponding well with the experimental values. Furthermore, the temperature dependence of RISC rate in THF and solid phase is shown in Figure 7, and the structural effect induced by

**Figure 7.** Temperature dependence of RISC rates for DBT-BZ-PXZ in THF (blue line) and solid phase (red line).

temperature is excluded in our calculation. As the temperature increases from 100 to 300 K, the RISC rate whether in THF or solid phase is significantly increased. This trend is more pronounced when the temperature exceeds 200 K. The calculations reasonably elucidate the experimental measurements. Thus, our theoretical investigations provide inner perspectives for nonradiative assumptions of excited state energy, and the TADF and AIE mechanisms are illustrated.

5. CONCLUSION

In this work, the photophysical properties of S_0 , S_1 , and T_1 are theoretically studied in the solid phase by the QM/MM

method. The geometrical changes between S_0 and S_1 in solid phase are restricted compared with those in THF. Besides, HR factors and reorganization energies are all decreased in solid phase, which is caused by the RIR effect for the low frequency twisting motion of dihedral angle θ_4 and RIV effect for the high frequency stretching motion of bond length B_4 . Thus, nonradiative consumptions of excited state energy are suppressed with the calculated total fluorescence efficiency Φ_F is 45.4% in solid phase, compared with that in THF ($\Phi_F = 0.0008\%$). This illustrates the AIE mechanism for DBT-BZ-PXZ. Furthermore, the calculated temperature dependence of RISC rate and the small energy gap ($\Delta E_{ST} = 0.06$ eV) between S_1 and T_1 are used to confirm the TADF mechanism. Moreover, T_1 state possesses HLCT feature both in THF and solid phase, and this transition property facilitates the RISC process by increasing the SOC constant and decreasing the energy gap ΔE_{ST} . Our calculations reasonably elucidate the experimental measurements, and help one to understand the TADF and AIE mechanisms of the DBT-BZ-PXZ molecule, which is beneficial for developing new efficient TADF emitters.

■ ASSOCIATED CONTENT

■ Supporting Information

The Supporting Information is available free of charge on the ACS Publications website at DOI: 10.1021/acs.jpcc.7b10238.

Figures showing a brief electroluminescence process, geometry comparisons between THF and the solid phase, and representation of the adiabatic potential energy surfaces and a table of oscillator strength, fluorescence rate, emission wavelength, and transition ratio from HOMO to LUMO (PDF)

■ AUTHOR INFORMATION

Corresponding Authors

*(C.-K.W.) E-mail: ckwang@sdu.edu.cn.

*(L.L.) E-mail: linll@sdu.edu.cn.

ORCID

Jianzhong Fan: 0000-0002-1524-0037

Lili Lin: 0000-0002-5319-713X

Notes

The authors declare no competing financial interest.

■ ACKNOWLEDGMENTS

This work is supported by the National Natural Science Foundation of China (Grant Nos. 11374195 and 21403133). Thanks are expressed for the support from the Taishan Scholar Project of Shandong Province and the Scientific Research Foundation of Shandong Normal University. Thanks are also given to the Promotive Research Fund for Excellent Young and Middle-aged Scientists of Shandong Province (Grant No. BS2014CL001) and a General Financial Grant from the China Postdoctoral Science Foundation (Grant No. 2014M560571). Great thanks are expressed to Professor Yi Luo, Professor Zhigang Shuai, and Qian Peng for their helpful suggestions in our calculation. Thanks are also given to Professor Yingli Niu for his great help in the usage of MOMAP.

■ REFERENCES

- (1) Tang, C. W.; VanSlyke, S. A. Organic electroluminescent diodes. *Appl. Phys. Lett.* **1987**, *51*, 913–915.
- (2) Reineke, S.; Lindner, F.; Schwartz, G.; Seidler, N.; Walzer, K.; Lussem, B.; et al. White organic light-emitting diodes with fluorescent tube efficiency. *Nature* **2009**, *459*, 234–238.
- (3) Adachi, C.; Baldo, M. A.; Thompson, M. E.; Forrest, S. R. Nearly 100% internal phosphorescence efficiency in an organic light-emitting device. *J. Appl. Phys.* **2001**, *90*, 5048–5051.
- (4) Baldo, M. A.; O'Brien, D. F.; You, Y.; Shoustikov, A.; Sibley, S.; Thompson, M. E.; et al. Highly efficient Phosphorescent emission from organic electroluminescent devices. *Nature* **1998**, *395*, 151–154.
- (5) Wu, C.; Guo, Q.; Ma, W.; Li, X.; Qiu, P.; Hu, J.; et al. Hybrid host materials for highly efficient electrophosphorescence and thermally activated delayed fluorescence independent of the linkage mode. *Phys. Chem. Chem. Phys.* **2017**, *19*, 5177–5184.
- (6) Masui, K.; Nakanotani, H.; Adachi, C. Analysis of exciton annihilation in high-efficiency sky-blue organic light-emitting diodes with thermally activated delayed fluorescence. *Org. Electron.* **2013**, *14*, 2721–2726.
- (7) Cao, S.; Hao, L.; Lai, W.-Y.; Zhang, H.; Yu, Z.; Zhang, X.; et al. Distinct phosphorescence enhancement of red-emitting iridium(III) complexes with formyl-functionalized phenylpyridine ligands. *J. Mater. Chem. C* **2016**, *4*, 4709–4718.
- (8) Qi, Y.; Zhao, J.; Wang, X.; Yu, J.; Chi, Z. High-efficiency phosphorescent organic light-emitting devices with low efficiency roll-off using a thermally activated delayed fluorescence material as host. *Org. Electron.* **2016**, *36*, 185–191.
- (9) Bai, Q.; Liu, H.; Yao, L.; Shan, T.; Li, J.; Gao, Y.; et al. Adjusting Nitrogen Atom Orientations of Pyridine Ring in Tetraphenylsilane-Based Hosts for Highly Efficient Blue Phosphorescent Organic Light-Emitting Devices. *ACS Appl. Mater. Interfaces* **2016**, *8*, 24793–24802.
- (10) Ye, H.; Zhou, K.; Wu, H.; Chen, K.; Xie, G.; Hu, J.; et al. Novel molecular host materials based on carbazole/PO hybrids with wide bandgap via unique linkages for solution-processed blue phosphorescent OLEDs. *Opt. Mater.* **2016**, *60*, 244–251.
- (11) Uoyama, H.; Goushi, K.; Shizu, K.; Nomura, H.; Adachi, C. Highly efficient organic light-emitting diodes from delayed fluorescence. *Nature* **2012**, *492*, 234–238.
- (12) Yu, L.; Wu, Z.; Zhong, C.; Xie, G.; Wu, K.; Ma, D.; et al. Tuning the emission from local excited-state to charge-transfer state transition in quinoxaline-based butterfly-shaped molecules: Efficient orange OLEDs based on thermally activated delayed fluorescence emitter. *Dyes Pigm.* **2017**, *141*, 325–332.
- (13) Zhang, Q. S.; Li, B.; Huang, S. P.; Nomura, H.; Tanaka, H.; Adachi, C. Efficient blue organic light-emitting diodes employing thermally activated delayed fluorescence. *Nat. Photonics* **2014**, *8*, 326–332.
- (14) Peng, Q.; Fan, D.; Duan, R.; Yi, Y.; Niu, Y.; Wang, D.; et al. Theoretical Study of Conversion and Decay Processes of Excited Triplet and Singlet States in a Thermally Activated Delayed Fluorescence Molecule. *J. Phys. Chem. C* **2017**, *121*, 13448–13456.
- (15) Tao, Y.; Yuan, K.; Chen, T.; Xu, P.; Li, H.; Chen, R.; Zheng, C.; Zhang, L.; Huang, W. Thermally activated delayed fluorescence materials towards the breakthrough of organoelectronics. *Adv. Mater.* **2014**, *26*, 7931–7958.
- (16) Zhao, B.; Zhang, T.; Chu, B.; Li, W.; Su, Z.; Luo, Y.; et al. Highly efficient tandem full exciplex orange and warm white OLEDs based on thermally activated delayed fluorescence mechanism. *Org. Electron.* **2015**, *17*, 15–21.
- (17) Liang, K.; Zheng, C.; Wang, K.; Liu, W.; Guo, Z.; Li, Y.; et al. Theoretical investigation of the singlet-triplet splittings for carbazole-based thermally activated delayed fluorescence emitters. *Phys. Chem. Chem. Phys.* **2016**, *18*, 26623–26629.
- (18) Wang, Y.; Zhang, G.; Gao, M.; Cai, Y.; Zhan, C.; Zhao, Z.; et al. Introductory lecture: recent research progress on aggregation-induced emission. *Faraday Discuss.* **2017**, *196*, 9–30.
- (19) Tsujimoto, H.; Ha, D.-G.; Markopoulos, G.; Chae, H. S.; Baldo, M. A.; Swager, T. M. Thermally Activated Delayed Fluorescence and Aggregation Induced Emission with Through-Space Charge Transfer. *J. Am. Chem. Soc.* **2017**, *139*, 4894–4900.

- (20) Fan, J.; Lin, L.; Wang, C.-K. Excited state properties of non-doped thermally activated delayed fluorescence emitters with aggregation-induced emission: a QM/MM study. *J. Mater. Chem. C* **2017**, *5*, 8390–8399.
- (21) Guo, J.; Li, X. L.; Nie, H.; Luo, W.; Gan, S.; Hu, S.; et al. Achieving High-Performance Nondoped OLEDs with Extremely Small Efficiency Roll-Off by Combining Aggregation-Induced Emission and Thermally Activated Delayed Fluorescence. *Adv. Funct. Mater.* **2017**, *27*, 1606458.
- (22) Huang, J.; Nie, H.; Zeng, J.; Zhuang, Z.; Gan, S.; Cai, Y.; et al. Highly Efficient Nondoped OLEDs with Negligible Efficiency Roll-Off Fabricated from Aggregation-Induced Delayed Fluorescence Luminescence. *Angew. Chem.* **2017**, *129*, 13151–13156.
- (23) Guo, J.; Li, X. L.; Nie, H.; Luo, W.; Hu, R.; Qin, A.; et al. Robust Luminescent Materials with Prominent Aggregation-Induced Emission and Thermally Activated Delayed Fluorescence for High-Performance Organic Light-Emitting Diodes. *Chem. Mater.* **2017**, *29*, 3623–3631.
- (24) Tomasi, J.; Mennucci, B.; Cammi, R. Quantum Mechanical Continuum Solvation Models. *Chem. Rev.* **2005**, *105*, 2999–3094.
- (25) Fan, J.; Cai, L.; Lin, L. L.; Wang, C.-K. Dynamics of Excited States for Fluorescent Emitters with Hybridized Local and Charge-Transfer Excited State in Solid Phase: A QM/MM Study. *J. Phys. Chem. A* **2016**, *120*, 9422–9430.
- (26) Wang, B.; Wang, X.; Wang, W.; Liu, F. Exploring the Mechanism of Fluorescence Quenching and Aggregation-Induced Emission of a Phenylethylene Derivative by QM (CASSCF and TDDFT) and ONIOM (QM:MM) Calculations. *J. Phys. Chem. C* **2016**, *120*, 21850–21857.
- (27) Sun, G.; Zhao, Y.; Liang, W. Aggregation-Induced Emission Mechanism of Dimethoxy-Tetraphenylethylene in Water Solution: Molecular Dynamics and QM/MM Investigations. *J. Chem. Theory Comput.* **2015**, *11*, 2257–2267.
- (28) Zheng, X.; Peng, Q.; Zhu, L.; Xie, Y.; Huang, X.; Shuai, Z. Unraveling the aggregation effect on amorphous phase AIE luminogens: a computational study. *Nanoscale* **2016**, *8*, 15173–15180.
- (29) Tao, Y.; Yuan, K.; Chen, T.; Xu, P.; Li, H.; Chen, R.; et al. Thermally activated delayed fluorescence materials towards the breakthrough of organoelectronics. *Adv. Mater.* **2014**, *26*, 7931–7958.
- (30) Shuai, Z.; Wang, D.; Peng, Q.; Geng, H. Computational evaluation of optoelectronic properties for organic/carbon materials. *Acc. Chem. Res.* **2014**, *47*, 3301–3309.
- (31) Shuai, Z.; Peng, Q. Excited states structure and processes: Understanding organic light-emitting diodes at the molecular level. *Phys. Rep.* **2014**, *537*, 123–156.
- (32) Peng, Q.; Niu, Y. L.; Shi, Q. H.; Gao, X.; Shuai, Z. G. Correlation Function Formalism for Triplet Excited State Decay: Combined Spin-Orbit and Nonadiabatic Couplings. *J. Chem. Theory Comput.* **2013**, *9*, 1132–1143.
- (33) Reimers, J. R. A Practical Method for the Use of Curvilinear Coordinates in Calculations of Normal-Mode-Projected Displacements and Duschinsky Rotation Matrices for Large Molecules. *J. Chem. Phys.* **2001**, *115*, 9103–9109.
- (34) Sun, H.; Zhang, S.; Zhong, C.; Sun, Z. Theoretical study of excited states of DNA base dimers and tetramers using optimally tuned range-separated density functional theory. *J. Comput. Chem.* **2016**, *37*, 684–693.
- (35) Penfold, T. J. On predicting the excited-state properties of thermally activated delayed fluorescence emitters. *J. Phys. Chem. C* **2015**, *119*, 13535–13544.
- (36) Huang, S.; Zhang, Q.; Shiota, Y.; Nakagawa, T.; Kuwabara, K.; Yoshizawa, K.; et al. Computational prediction for singlet- and triplet-transition energies of charge-transfer compounds. *J. Chem. Theory Comput.* **2013**, *9*, 3872–3877.
- (37) Chen, T.; Zheng, L.; Yuan, J.; An, Z.; Chen, R.; Tao, Y. Understanding the control of singlet-triplet splitting for organic exciton manipulating: a combined theoretical and experimental approach. *Sci. Rep.* **2015**, *5*, 10923.
- (38) Fan, J. Z.; Qiu, S.; Lin, L.; Wang, C. K. First-Principles Investigation on Triazine Based Thermally Activated Delayed Fluorescence Emitters. *Chin. J. Chem. Phys.* **2016**, *29*, 291–296.
- (39) Fan, J. Z.; Lin, L. L.; Wang, C. K. Decreasing the singlet–triplet gap for thermally activated delayed fluorescence molecules by structural modification on the donor fragment: First-principles study. *Chem. Phys. Lett.* **2016**, *652*, 16–21.
- (40) Chung, L. W.; Sameera, W. M.; Ramozzi, R.; Page, A. J.; Hatanaka, M.; Petrova, G. P.; et al. The ONIOM Method and Its Applications. *Chem. Rev.* **2015**, *115*, 5678–5796.
- (41) Frisch, M. J.; Trucks, G. W.; Schlegel, H. B.; Scuseria, G. E.; Robb, M. A.; Cheeseman, J. R. et al. *Gaussian 09*, revision D01; Gaussian, Inc.: Wallingford, CT; 2013.
- (42) Johnson, E. R.; Keinan, S.; Mori-Sánchez, P.; Contreras-García, J.; Cohen, A. J.; Yang, W. Revealing Noncovalent Interactions. *J. Am. Chem. Soc.* **2010**, *132*, 6498–6506.
- (43) Lu, T.; Chen, F. W. Multiwfn: a multifunctional wavefunction analyzer. *J. Comput. Chem.* **2012**, *33*, 580–592.
- (44) Gibson, J.; Penfold, T. J. Nonadiabatic coupling reduces the activation energy in thermally activated delayed fluorescence. *Phys. Chem. Chem. Phys.* **2017**, *19*, 8428–8434.
- (45) Etherington, M. K.; Gibson, J.; Higginbotham, H. F.; Penfold, T. J.; Monkman, A. P. Revealing the spin-vibronic coupling mechanism of thermally activated delayed fluorescence. *Nat. Commun.* **2016**, *7*, 13680.
- (46) Gibson, J.; Monkman, A. P.; Penfold, T. J. The Importance of Vibronic Coupling for Efficient Reverse Intersystem Crossing in Thermally Activated Delayed Fluorescence Molecules. *ChemPhysChem* **2016**, *17*, 2956–2961.
- (47) DALTON. A molecular electronic structure program, release Dalton 2011. <http://daltonprogram.org/>.